Nanoscale

ROYAL SOCIETY OF CHEMISTRY

PAPER

View Article Online
View Journal

Check for updates

Cite this: DOI: 10.1039/d0nr01858a

Ion transport across solid-state ion channels perturbed by directed strain†

A. Smolyanitsky, * A. Fang, ‡ A. F. Kazakov and E. Paulechka

Received 5th March 2020,
Accepted 27th April 2020

DOI: 10.1039/d0nr01858a

rsc.li/nanoscale

We combine quantum-chemical calculations and molecular dynamics simulations to consider aqueous ion flow across non-axisymmetric nanopores in monolayer graphene and MoS_2. When the pore-containing membrane is subject to uniaxial tensile strains applied in various directions, the corresponding permeability exhibits considerable directional dependence. This anisotropy is shown to arise from directed perturbations of the local electrostatics by the corresponding pore deformation, as enabled by the pore edge geometries and atomic compositions. By considering nanopores with ionic permeability that depends on the strain direction, we present model systems that may yield a detailed understanding of the structure–function relationship in solid-state and biological ion channels. Specifically, the observed anisotropic effects potentially enable the use of permeation measurements across strained membranes to obtain directional profiles of ion–pore energetics as contributed by groups of atoms or even individual atoms at the pore edge. The resulting insight may facilitate the development of subnanoscale pores with novel functionalities arising from locally asymmetric pore edge features.

Published on 28 April 2020. Downloaded on 5/5/2020 6:39:12 AM.

Introduction

Control of solvated ion flow across nanoporous solid-state membranes is key to a wide range of nanofluidics applications, ranging from drug delivery[1] to energy storage.[2] In most cases, external gating of ionic permeation and selectivity is enabled by modifying the ion–pore interactions and/or the local thermodynamics. As a result, the main gating mechanisms include electrostatic gating,[3–6] enzymatic-like processes,[7] or changes in system temperature.[8,9] In addition, 2D-material-based ion channels sensitively gated by tensile mechanical strain applied to the membrane were recently predicted.[10,11]

Strain-gated control of ion flow across crown-like pores in graphene[10,12] and subnanoscale atomically symmetric multivacancies in molybdenum disulfide (MoS_2)[11] generally owes to the exceptionally high pore confinement experienced by the permeating ions. For ion–trapping pores (*e.g.*, graphene-embedded crown ethers), ion–pore and ion–solvent electrostatic interactions actively compete inside the pore and this competition is controlled by moderate pore dilation. As a result, order-of-magnitude permeability changes in response to few-percent strain are observed. For pores that do not trap ions, general ion–pore repulsion is reduced by pore dilation, also resulting in high mechanosensitivity.[11]

In the case of isotropic strains applied to ideal crown pores featuring hexagonal edge symmetry, the edge atoms essentially form a circle around the ion located in the center of the pore. Consequently, pore dilation is assumed to be radial throughout the pore edge. Moreover, hexagonal symmetry yields nearly identical permeability responses to *uniaxial* tensile strains applied along different directions.[10] More generally, the assumption of a nearly circular pore edge underlies the well-accepted paradigm of ion–pore interactions, in which the pore is assumed to interact with permeating ions as a single isotropic entity. In the case of a non-axisymmetric pore edge lining, however, isotropy is not expected. The asymmetry within the pore edge can arise from different electrostatic charges carried by the edge atoms regardless of the pore shape, as well as from non-circular edge geometries (*e.g.*, triangular[13–16] or diamond-shaped[11] pores), as discussed in detail later. Given that in experiments, subnanoscale pores may not always have an axisymmetric structure, characterizing ion–pore interactions beyond the assumption of a circular edge may lead to a more focused understanding of structure–function relationships in subnanoscale pores.

Here, using quantum-chemical calculations and molecular dynamics (MD) simulations, we demonstrate examples of pores with marked anisotropy in their response to uniaxial strain, depending on its direction. We discuss the basic properties of the observed anisotropy, as determined by electrostatic and geometric effects. Finally, we demonstrate that per-

Applied Chemicals and Materials Division, National Institute of Standards and Technology, Boulder, CO 80305, USA. E-mail: alex.smolyanitsky@nist.gov

†Electronic supplementary information (ESI) available. See DOI: 10.1039/d0nr01858a

‡Present address: BIOVIA, Dassault Systèmes, San Diego, CA, USA.

Published on 28 April 2020. Downloaded on 5/5/2020 6:39:12 AM.

meation measurements across membranes subject to perturbative strains applied along various directions potentially enable obtaining directional profiles of the ion–pore interactions beyond the assumption of a uniform pore edge. In particular, for pores where short-range ion–pore interactions dominate, the resulting profiles are shown to contain features contributed by groups of atoms at the pore edge.

Ionic flow across various porous membranes was MD-simulated here, and one representative example is shown in Fig. 1. The system consists of a 5.6 nm × 6.4 nm monolayer graphene membrane featuring nine identical subnanoscale pores. The membrane is immersed in a room-temperature (T = 300 K) aqueous solution of 0.5 M KCl in a 5 nm-tall periodic simulation cell. The ion flow is driven by a constant electric field E_z = 0.05 V nm^{-1}, roughly corresponding to a transmembrane voltage of 0.05 V nm^{-1} × 5 nm = 0.25 V. The resulting currents are calculated from ion fluxes as described in our previous works.[10,11,17] The simulation setup uses the standard OPLS-AA framework,[18,19] identical to those in our previous works.[10,17] Uniaxial in-plane tensile strains are applied to the membrane as described earlier[10] and in the ESI.† Strain magnitudes are varied up to 0.04, well within graphene's experimentally observed limits of elasticity.[20]

As shown in the upper right corner of Fig. 1, the pore structure is similar to a graphene-embedded crown ether[17,21] and is expected to trap solvated alkali metal ions. The important difference is that, instead of six edge oxygen atoms, only two edge atoms are oxygen atoms (red), while the rest are nitrogen atoms (blue). We refer to this pore as N_4O_2 in the text below. As discussed earlier,[10,17] ion–pore interactions are those between the ion and a total of six radially oriented dipoles formed by the edge atom (N or O) and the two neighboring carbons. Within the MD framework, the dipole, as enclosed in the dashed triangles in Fig. 1, is described by the atomic charge Q_i of the edge atom (i is N or O) and two $-Q_i/2$ charges of the two nearest carbons. If we posit that Q_O and Q_N are sufficiently different due to the differences in N–C_2 and O–C_2 bonding, there should arise a considerable anisotropy in the distortion of pore electrostatics, depending on the direction of externally applied uniaxial strain. On geometric grounds, for the pores in Fig. 1, this anisotropy should be maximal between strains applied along X and Y. Reasonable estimates of the atomic charges at the pore edge are key here. In addition to generally governing permeability[22] and mechanosensitivity,[12] these charge values should directly control the degree of potential anisotropy. We therefore used the Gaussian 16 package[23] to perform quantum-chemical calculations and obtain the partial atomic charges according to the OPLS-AA-compatible CHELPG scheme.[24] The calculations were performed at the HF/6-31+G(d) theory level.[25,26] The obtained charges (in the units of elementary charge) are Q_O = −0.26 and Q_N = −0.64, while each atom in the corresponding nearest-neighbor carbon pair carries charge of +0.13 and +0.32, respectively. Our main results were obtained with these charges. In addition, using the CP2K package,[27] we performed DFT calculations to obtain the DDAP atomic charges.[28] These calculations, set up using the PBE exchange functional,[29] Gaussian plane-wave pseudopotentials,[30] and the DZVP basis set,[31] yielded Q_O = −0.23 and Q_N = −0.48. The results obtained with these charges are provided in the section S1 of the ESI.† We note that in our MD simulations the values of partial atomic charges (from both CHELPG and DDAP) are assumed to be constant with respect to the membrane strain. This assumption greatly simplifies simulation setup and enables a

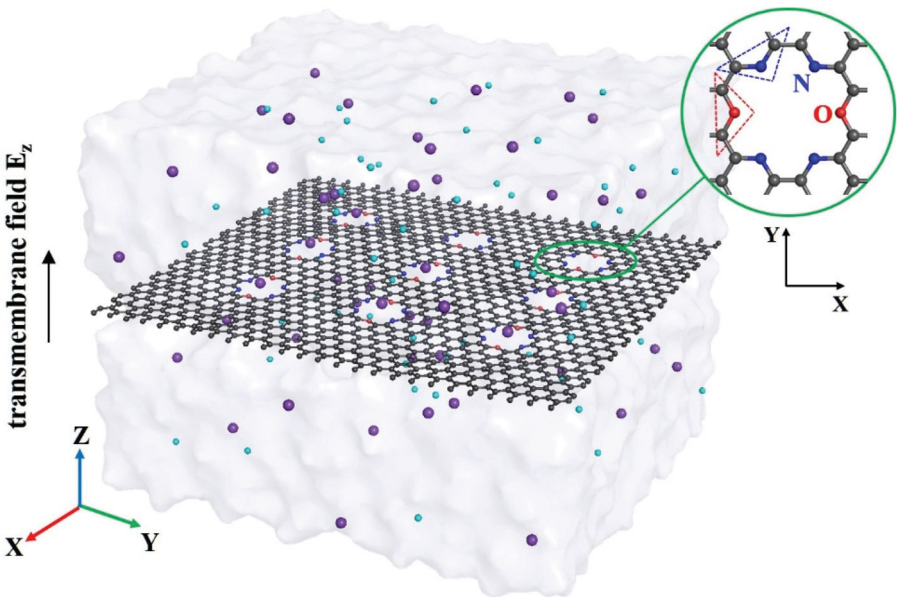

Fig. 1 An example of simulated system: graphene membrane featuring nine pores in an aqueous ionic environment. Water and ions are shown as light-purple surface and bright spheres, respectively. The pore structure is shown in the upper right corner; the dashed triangles enclose the atoms forming pore edge dipoles.

This journal is © The Royal Society of Chemistry 2020

Published on 28 April 2020. Downloaded on 5/5/2020 6:39:12 AM.

standard MD workflow. As estimated in section S1 of the ESI† for the DDAP charges, average atomic charge magnitudes in the DFT simulations varied by ~3.2% per 1% of isotropic strain. However, we expect that this level of charge variability would be unlikely to affect the qualitative nature of the results presented here.[22]

Results

The ionic currents across graphene-embedded N_4O_2 pores described above were simulated for various strains, and the results are presented in Fig. 2. Indeed, the N_4O_2 structure exhibits different levels of mechanosensitivity, depending on the direction of strain, while biaxial isotropic strain expectedly causes the largest changes in ionic permeation. As described in our previous work,[10] an estimate of the ion current as a function of strain ε is $I(\varepsilon) = I_0 e^{\mu}$, where $\mu = \frac{1}{k_B T}\left(\frac{dU}{d\varepsilon}\right)$ is dimensionless sensitivity to strain. Above, $U \approx U_{\text{ion–pore}} + U_{\text{ion–water}}$ approximates the total free energy of electrostatic interactions for an aqueous ion trapped in the pore; k_B and T are the Boltzmann constant and system temperature, respectively. In the differential limit of small strains, $\left(\frac{dU}{d\varepsilon}\right)$ is assumed to be constant. Fitting the data in Fig. 2 yields μ_{XX} = 45.80, μ_{YY} = 68.57, and μ_{XY} = 102.54. The sensitivity to biaxial strain $\mu_{XY} \approx \mu_{XX} + \mu_{YY}$ is well-expected and consistent with earlier results,[10] while the difference between μ_{YY} and μ_{XX} is of our current interest.

The curves fitted to *XX* and *YY* data in Fig. 2 yield an ion permeation anisotropy factor $\kappa_{YX} = I_{YY}/I_{XX}$ reaching ~3 at higher strains, consistent with $\kappa_{YX} \approx e^{(\mu_{YY}-\mu_{XX})\varepsilon} = 2.5$ at $\varepsilon = 0.04$. To describe the underlying mechanism we recall that, from the definition above, the *Y*–*X* permeation anisotropy can be expressed as

$$\kappa_{YX} \approx e^{\frac{\delta U_{YX}}{k_B T}}, \quad (1)$$

where

$$\delta U_{YX} = (\delta U^{YY}_{\text{ion–pore}} - \delta U^{XX}_{\text{ion–pore}}) + (\delta U^{YY}_{\text{ion–water}} - \delta U^{XX}_{\text{ion–water}}) \quad (2)$$

is the asymmetry in the corresponding free energy's response to the selected uniaxial strain directions. A naïve guess is that the ion–water asymmetry component in eqn (2) is negligible. Given the data in Fig. 2, δU_{YX} should not exceed $k_B T \approx 2.5$ kJ mol^{-1} within the presented strain range. However, the ion–pore component reaches $(\delta U^{YY}_{\text{ion–pore}} - \delta U^{XX}_{\text{ion–pore}}) \sim 10$ kJ mol^{-1} at $\varepsilon = 0.04$ (see section S2 in the ESI†), corresponding to $\kappa_{YX} \approx 55$, far in excess of the data in Fig. 2. We therefore believe that $(\delta U^{YY}_{\text{ion–water}} - \delta U^{XX}_{\text{ion–water}})$ significantly opposes the "vacuum" ion–pore component. This hypothesis is supported by the MD-simulated ion–pore and ion–water energy asymmetries in Fig. 3. Because the ion–water energies have an average estimated uncertainty of $\sim 2k_B T$, an independent measure of ion–water interactions is necessary. It is presented in the inset of Fig. 3 in the form of ion–water first shell coordination numbers N_c, obtained as integrals of the corresponding radial distribution functions (RDFs) (see section S3 of the ESI† for

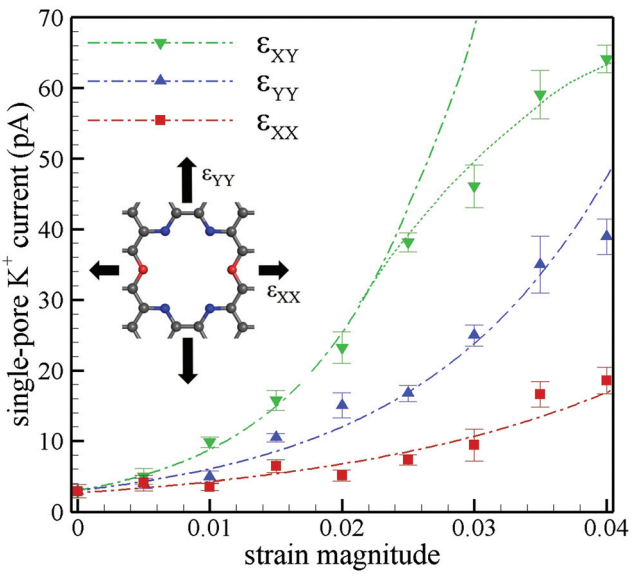

Fig. 2 Single-pore K^+ currents as a function of membrane strains applied along the *X*, *Y*, and *XY* directions, where *XY* indicates isotropic ($\varepsilon_{XX} = \varepsilon_{YY}$) biaxial stretching. Each ion current value was obtained from the ionic flux simulated for 150 ns. No Cl^- permeation was observed. The dash-dotted lines are exponential fits to simulated data. For *XY*-stretching, only the data points corresponding to $\varepsilon \leq 0.025$ were used for fitting due to saturation of the mechanosensitive effect for $\varepsilon > 0.025$ (dotted green curve).

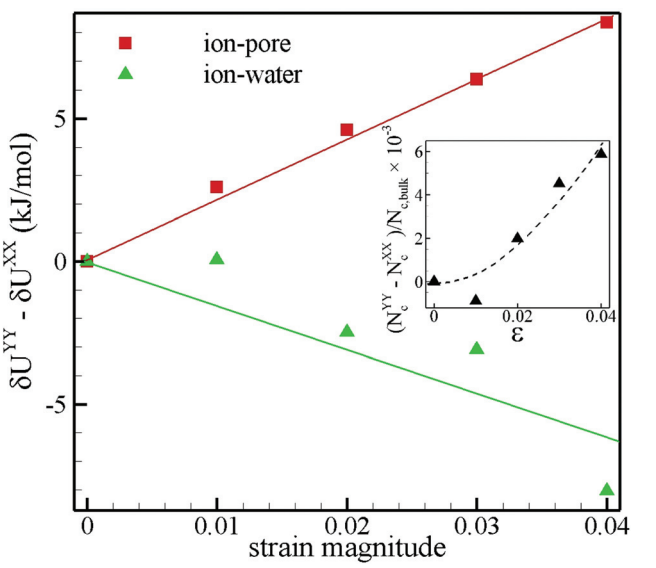

Fig. 3 Simulated ion–pore and ion–water interaction energy anisotropies as functions of uniaxial strain. Each energy point was simulated for 50 ns. Solid lines are linear fits added as visual guides. All simulated energy values are negative (relative to vacuum), so the shown increasing and decreasing trends correspond to reduction and increase in interaction strengths, respectively. The inset shows anisotropy in the response of coordination numbers (integrated ion–water RDFs) to uniaxial strain.

Published on 28 April 2020. Downloaded on 5/5/2020 6:39:12 AM.

details). As shown, $N_c^{YY} - N_c^{XX}$ increases with ε, confirming the ion–water energy trend.

Granted, it has been shown that the solvent moderates the overall level of mechanosensitivity in graphene-embedded crowns, whereby pore dilation leads to *reduction* in the ion–pore component and an *increase* in the ion–water component. The effect is essentially strain-dependent solvent screening in confinement.[10] Here, however, a direct argument based on the reduction of confinement is problematic, because on geometric grounds uniaxial membrane strains along X and Y direction dilate the pores nearly identically (see section S2 of the ESI† and ref. 10). The solvent's moderating effect on δU has a more subtle explanation in this case. As estimated in the ESI† of ref. 10, $U_{\text{ion–water}}$ is an overall *increasing function of how much a pore-trapped ion fluctuates out of the pore plane*. Note that the RMSD of these fluctuations $\propto \sqrt{\frac{k_B T}{k_{\text{ion–pore}}}}$, where $k_{\text{ion–pore}}$ is the effective ion–pore force constant – an *increasing function of* the electrostatic potential well depth $|U_{\text{ion–pore}}|$. This RMSD is essentially a measure of how much the ion is thermally "peeking" into the solvent, which *increases with decreasing ion–pore interaction strength.*[10] Therefore, *any* reduction of the ion–pore interactions generally contributes toward increasing ion–water component. Consequently, anisotropy in the $U_{\text{ion–pore}}$ component *causes* a contribution toward opposing anisotropy in the $U_{\text{ion–water}}$ component. We also note that the anisotropy observed here is generally subject to thermal smearing and, given eqn (1), is expected to decrease with increasing system temperature (see section S6 of the ESI†).

So far, we have discussed uniaxial strains in the X and Y direction. In order to investigate N_4O_2 pores' response to uniaxial strain of a given magnitude applied at an arbitrary angle φ (*e.g.*, relative to the X-direction), we have developed a procedure that deforms the membrane in an appropriate triclinic simulation box (see details in section S4 of the ESI†). Using this approach, we applied uniaxial strains in angle sweeps $0° \leq \varphi \leq 90°$ to cover the full angular range of the pore edge asymmetry. The results are shown in Fig. 4.

For all presented values of ε, the permeability of N_4O_2 pores increases continuously with increasing φ. In contrast, for the 18-crown-6 pore, the curve is nearly circular, expectedly corresponding to an isotropic case. Such a continuous response for the N_4O_2 pore is not surprising, given the gradually increasing electrostatic contribution from the displacements of nitrogen atoms carrying larger atomic charges, as φ increases to 90°. Consider an ion trapped and traversing the pore near coordinates (0, 0) in the pore plane and surrounded by edge pore atoms indexed by i and located at $\boldsymbol{r_i}$. The first-order electrostatic ion–pore component of δU in response to an arbitrary uniaxial strain tensor $\boldsymbol{\varepsilon}$ is proportional to the projections of the atomic displacements upon the corresponding $\boldsymbol{r_i}$ as $\sum_i \frac{Q_i}{r_i^3}(\boldsymbol{\delta L_i}(\boldsymbol{\varepsilon}, \boldsymbol{r_i}) \cdot \boldsymbol{r_i})$. The sum is over all pore edge atoms. Above, $\boldsymbol{\delta L_i}(\boldsymbol{\varepsilon},\boldsymbol{r_i})$ is the i-th atom's strain-induced displacement calculated from the corresponding *per-atom tensor*, specific to the mechanical properties of the pore edge in a given membrane material. For a pore with fully uniform in-plane response (of the isotropic host membrane, for instance), $\boldsymbol{\delta L_i}$ is calculated in the ESI eqn (S11).† Changes in the higher-order electrostatic contributions (*e.g.*, in the form of Lennard-Jones potential in MD simulations) have a similar dependence, except with higher powers of r_i in the denominator. It is evident that, aside from the mechanical response of the material and the pore edge, the sources of anisotropy include both the charge values of the pore edge atoms Q_i and the distances from the ion r_i. For ion–pore interactions dominated by Coulomb electrostatics, the directions of maximum response

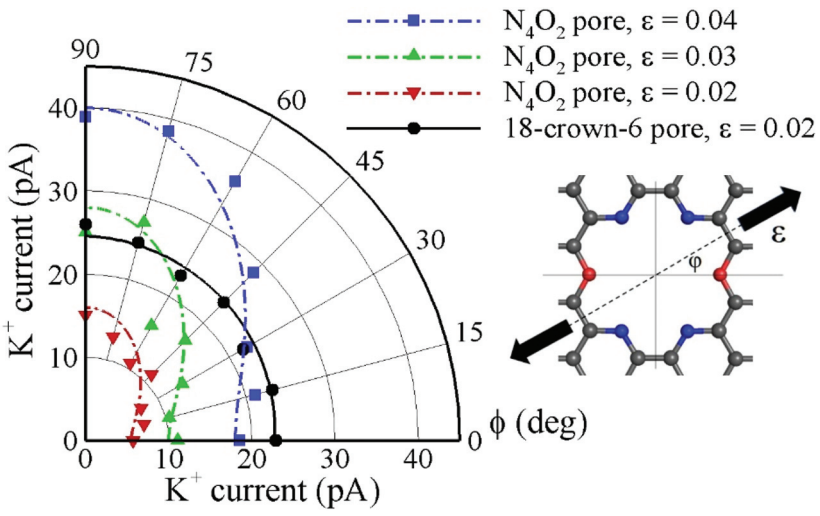

Fig. 4 A family of polar curves describing K^+ permeation across graphene-embedded N_4O_2 pores as a function of uniaxial strain's direction, at various strain magnitudes. Each conduction point was simulated for 150 ns. In addition to the N_4O_2 pores, permeation *via* uniaxially strained 18-crown-6 pores is presented as an example of isotropic response (black circles and solid line). All continuous lines are $A \exp(B \cos \varphi)$-type fits to simulated data, added as visual guides. The corresponding data uncertainties are of the same order as the vertical bars shown in Fig. 2.

 This journal is © The Royal Society of Chemistry 2020

Published on 28 April 2020. Downloaded on 5/5/2020 6:39:12 AM.

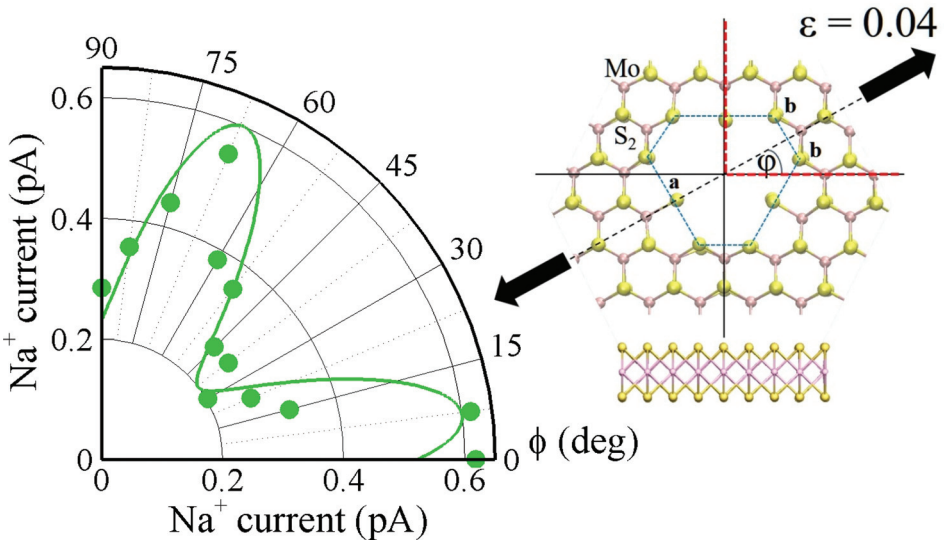

Fig. 5 Ion-repulsive diamond-shaped pores in monolayer MoS_2 and the polar curve describing single-pore Na^+ permeation as a function of φ. The pore edge contour is provided by the dashed blue line. Permeation points were simulated at ε = 0.04 for 400 ns to 1600 ns per point and the average data uncertainty is 0.1 pA. The solid line is a visual guide of similar functional form as in Fig. 4. Dashed red lines outline the angular range of applied strains ($0° \leq \varphi \leq 90°$), which is roughly three times the observed response range.

to uniaxial strain correspond to groups of atoms with the largest Q_i magnitudes and the shortest r_i. One should not expect particularly sharp angular regions of minima or maxima in the response dominated by $1/r$ electrostatics, due to considerable contributions by *groups of edge atoms* and not individual atoms. As a result, the polar plots in Fig. 4 should be viewed as locally "smeared" energetic profiles of the pore edge.

It should now be clear that the directional response to uniaxial tensile strain arises from inhomogeneous pore edge charges and the pore geometry itself. Thus far, we have only considered directional anisotropy arising from a non-axisymmetric distribution of the relatively long-range first-order electrostatics along the pore edge. Non-circular pores in hexagonal boron nitride[13,14] or triangular[15,16] and diamond-shaped[11] pores in monolayer MoS_2 are marked by strong higher-order electrostatics and present another potentially interesting case. For example, let us consider the directional response of the diamond-shaped pores in MoS_2.[11] As demonstrated earlier, these pores generally repel ions and feature significant atomic charge variation, depending on the edge atom location.[11] We performed an angular sweep of uniaxial strain (ε = 0.04) applied to a monolayer MoS_2 membrane featuring nine such pores. The simulation setup with 0.5 M of aqueous NaCl was similar to that described above for graphene-embedded N_4O_2 pores and used a refined parameter set[32] utilized in our earlier work.[11] Pore geometry and the simulated angular range are shown in Fig. 5, along with the permeability data. Anisotropy of order ~3, similar to that in Fig. 2 and 4, is observed. The angular range of permeation variability, however, is significantly narrower: the minima and maxima are separated by 30°, which is 1/3 of the corresponding range for N_4O_2 pores. This response cannot be explained based on the first-order electrostatics alone (in Fig. 5, atoms labeled **a** and **b** carry charges −0.022 and −0.33, respectively[11]). We therefore suggest that the short-range interactions, already known to underlie the repulsive nature of these pores,[11] are mostly responsible for the relatively sharp angular features of the response. Consequently, for non-circular pores with a strong short-range component in the ion–pore interactions, the directional response to strain appears to yield ion–pore energy profiles with nearly atomistic detail. Interestingly, such profiles may yield information about any parasitic pre-strain inevitably present in the pores. See section S7 of the ESI† for further details.

Conclusions

We have shown that the ionic permeability of non-axisymmetric subnanoscale pores may have a sizeable dependence on the direction of uniaxial tensile strain applied to the membrane. The sources of anisotropy include inhomogeneity in the atomic charge distribution along the pore edge, as well as edge geometry. For the graphene-embedded hexagonal N_4O_2 pores that feature asymmetry in Coulomb interactions, the ion permeation is shown to change by a factor of ~3 within a 90-degree range of strain directions. For the diamond-shaped pores in monolayer MoS_2, where short-range repulsive interactions dominate, a similar degree of anisotropy is observed within a 30-degree range. As a result, nearly atomistic maps of the pore edge energetics may be obtained from macroscopic measurements of ionic permeability.

The obtained results suggest the possibility of "smart" membranes that significantly change their ionic permeability,

Published on 28 April 2020. Downloaded on 5/5/2020 6:39:12 AM.

depending on the direction of moderate tensile stretching. Because relatively minor energy changes ($\delta U \sim k_B T$) translate into sizeable current modifications *via* the corresponding Arrhenius exponent, our results may enable a path toward a detailed understanding of how ions interact with subnanoscale pores, including biological ion channels. In particular, the reported angular anisotropy suggests the possibility of probing energy contributions not only from the entire pore, but also *from groups of pore edge atoms, or even individual atoms*, depending on the pore geometry and the dominating type of interactions. In addition, exploring the moderating solvent effects on mechanosensitivity in general and in the context of anisotropy presented here may enable a better understanding of solvent screening in subnanoscale confinement. Finally, novel pore functionalities may be obtained from functionalization of portions of the pore lining, as well as from mere pore lining defects.

It is important to note that in membranes featuring pore arrays, observation of the phenomena predicted here requires not only control over the pore structure, but also identical/equivalent pore orientation relative to the host lattice. Therefore, without doubt, it will be challenging to experimentally verify our predictions, both in terms of membrane fabrication and precise application of strains. Nonetheless, recent advances in fabrication[15,16] and strain actuation at the nanoscale[20,33] suggest that rapid progress is being made toward the possibility of experimentally exploring strain-gated nanofluidic systems.

Disclaimer

This work is a contribution of the National Institute of Standards and Technology, an agency of the US government. Not subject to copyright in the USA. Trade names are provided only to specify procedures adequately and do not imply endorsement by the National Institute of Standards and Technology. Similar products by other manufacturers may be found to work as well or better.

Conflicts of interest

There are no conflicts to declare.

Acknowledgements

The authors thank K. Kroenlein for devising and implementing data processing software. We are also grateful to C. Muzny and D. Luchinsky for enlightening discussions.

Part of this research was performed while A. Fang held a National Research Council (NRC) Postdoctoral Research Associateship at the National Institute of Standards and Technology (NIST). Authors gratefully acknowledge support from the Materials Genome Initiative.

References

1 R. Duan, F. Xia and L. Jiang, Constructing Tunable Nanopores and Their Application in Drug Delivery, *ACS Nano*, 2013, **7**(10), 8344–8349.
2 H. G. Park and Y. Jung, Carbon nanofluidics of rapid water transport for energy applications, *Chem. Soc. Rev.*, 2014, **43**(2), 565–576.
3 P. Joshi, *et al.*, Field effect modulation of ionic conductance of cylindrical silicon-on-insulator nanopore array, *J. Appl. Phys.*, 2010, **107**(5), 054701.
4 W. Guan, R. Fan and M. A. Reed, Field-effect reconfigurable nanofluidic ionic diodes, *Nat. Commun.*, 2011, **2**, 506.
5 W. Guan and M. A. Reed, Electric Field Modulation of the Membrane Potential in Solid-State Ion Channels, *Nano Lett.*, 2012, **12**(12), 6441–6447.
6 A. Smolyanitsky and M. Saraniti, Silicon nanopores as bioelectronic devices: a simulation study, *J. Comput. Electron.*, 2010, **8**(2), 90–97.
7 G. Pérez-Mitta, *et al.*, Highly Sensitive Biosensing with Solid-State Nanopores Displaying Enzymatically Reconfigurable Rectification Properties, *Nano Lett.*, 2018, **18**(5), 3303–3310.
8 L. Payet, *et al.*, Temperature Effect on Ionic Current and ssDNA Transport through Nanopores, *Biophys. J.*, 2015, **109**(8), 1600–1607.
9 Y. Zhou, *et al.*, High-Temperature Gating of Solid-State Nanopores with Thermo-Responsive Macromolecular Nanoactuators in Ionic Liquids, *Adv. Mater.*, 2012, **24**(7), 962–967.
10 A. Fang, *et al.*, Highly mechanosensitive ion channels from graphene-embedded crown ethers, *Nat. Mater.*, 2019, **18**(1), 76–81.
11 A. Fang, K. Kroenlein and A. Smolyanitsky, Mechanosensitive Ion Permeation across Subnanoporous MoS_2 Monolayers, *J. Phys. Chem. C*, 2019, **123**(6), 3588–3593.
12 S. Sahu, *et al.*, Optimal transport and colossal ionic mechano-conductance in graphene crown ethers, *Sci. Adv.*, 2019, **5**(7), eaaw5478.
13 O. Cretu, *et al.*, Structure and Local Chemical Properties of Boron-Terminated Tetravacancies in Hexagonal Boron Nitride, *Phys. Rev. Lett.*, 2015, **114**(7), 075502.
14 S. M. Gilbert, *et al.*, Fabrication of Subnanometer-Precision Nanopores in Hexagonal Boron Nitride, *Sci. Rep.*, 2017, **7**(1), 15096.
15 J. P. Thiruraman, *et al.*, Angstrom-Size Defect Creation and Ionic Transport through Pores in Single-Layer MoS_2, *Nano Lett.*, 2018, **18**(3), 1651–1659.
16 J. Feng, *et al.*, Electrochemical Reaction in Single Layer MoS_2: Nanopores Opened Atom by Atom, *Nano Lett.*, 2015, **15**(5), 3431–3438.
17 A. Smolyanitsky, E. Paulechka and K. Kroenlein, Aqueous Ion Trapping and Transport in Graphene-Embedded 18-Crown-6 Ether Pores, *ACS Nano*, 2018, **12**(7), 6677–6684.
18 W. L. Jorgensen and J. Tirado-Rives, The OPLS [optimized potentials for liquid simulations] potential functions for

 This journal is © The Royal Society of Chemistry 2020

Published on 28 April 2020. Downloaded on 5/5/2020 6:39:12 AM.

proteins, energy minimizations for crystals of cyclic peptides and crambin, *J. Am. Chem. Soc.*, 1988, **110**(6), 1657–1666.

19 W. L. Jorgensen, D. S. Maxwell and J. Tirado-Rives, Development and Testing of the OPLS All-Atom Force Field on Conformational Energetics and Properties of Organic Liquids, *J. Am. Chem. Soc.*, 1996, **118**(45), 11225–11236.

20 K. Cao, *et al.*, Elastic straining of free-standing monolayer graphene, *Nat. Commun.*, 2020, **11**(1), 284.

21 J. Guo, *et al.*, Crown ethers in graphene, *Nat. Commun.*, 2014, **5**, 5389.

22 C. Guardiani, *et al.*, Exploring the pore charge dependence of K^+ and Cl– permeation across a graphene monolayer: a molecular dynamics study, *RSC Adv.*, 2019, **9**(35), 20402–20414.

23 M. J. Frisch, *et al.*, *Gaussian 16 Rev. C.01*, Wallingford, CT, 2016.

24 C. M. Breneman and K. B. Wiberg, Determining atom-centered monopoles from molecular electrostatic potentials. The need for high sampling density in formamide conformational analysis, *J. Comput. Chem.*, 1990, **11**(3), 361–373.

25 C. Lee, W. Yang and R. G. Parr, Development of the Colle-Salvetti correlation-energy formula into a functional of the electron density, *Phys. Rev. B: Condens. Matter Mater. Phys.*, 1988, **37**(2), 785–789.

26 A. D. Becke, Density-functional thermochemistry. III. The role of exact exchange, *J. Chem. Phys.*, 1993, **98**(7), 5648–5652.

27 J. Hutter, *et al.*, cp2k: atomistic simulations of condensed matter systems, *Wiley Interdiscip. Rev.: Comput. Mol. Sci.*, 2014, **4**(1), 15–25.

28 P. E. Blöchl, Electrostatic decoupling of periodic images of plane-wave-expanded densities and derived atomic point charges, *J. Chem. Phys.*, 1995, **103**(17), 7422–7428.

29 J. P. Perdew, K. Burke and M. Ernzerhof, Generalized Gradient Approximation Made Simple, *Phys. Rev. Lett.*, 1996, **77**(18), 3865–3868.

30 C. Hartwigsen, S. Goedecker and J. Hutter, Relativistic separable dual-space Gaussian pseudopotentials from H to Rn, *Phys. Rev. B: Condens. Matter Mater. Phys.*, 1998, **58**(7), 3641–3662.

31 J. VandeVondele and J. Hutter, Gaussian basis sets for accurate calculations on molecular systems in gas and condensed phases, *J. Chem. Phys.*, 2007, **127**(11), 114105.

32 V. Sresht, *et al.*, Quantitative Modeling of MoS_2–Solvent Interfaces: Predicting Contact Angles and Exfoliation Performance using Molecular Dynamics, *J. Phys. Chem. C*, 2017, **121**(16), 9022–9031.

33 M. Goldsche, *et al.*, Tailoring Mechanically Tunable Strain Fields in Graphene, *Nano Lett.*, 2018, **18**(3), 1707–1713.